Propagation Properties of Annular Beam Array for Uplink Satellite Links

Muhsin Caner Gökçe and Rudolf Saathof

***Abstract*—The spatial diversity and beam shaping are key approaches to mitigating the effects of atmospheric turbulence on laser beam propagation through free space. This study investigates the propagation characteristics of an annular beam array in atmospheric turbulence for uplink satellite links using the extended Huygens–Fresnel principle and the Rytov method. Analytical derivations are presented for various optical parameters, including received intensity, kurtosis parameter, beam footprint size, Strehl ratio, beam wander, scintillation index, and bit error rate (BER), to evaluate the beam performance under turbulence conditions. The findings indicate that converting a Gaussian beam into an annular shape enhances performance, with further improvements observed as the number of beams increases.**

***Index Terms*—Atmospheric turbulence, beam shaping, beam size, intensity, kurtosis, optical wave propagation, spatial diversity, Strehl ratio.**

I. Introduction

FREE-SPACE optical communication provides high-bandwidth, unlicensed wireless connectivity with cost advantages over traditional radio frequency (RF) solutions. However, practical deployment faces significant challenges from atmospheric conditions. Particularly, weather-induced scattering (rain, fog, and snow) and turbulence effects can dramatically reduce link reliability and performance. These systems can be categorized based on their transmission range, spanning from short-distance interchip connections to inter-vehicular, interbuilding, ground-to-satellite, intersatellite, and even interplanetary communications with relay links [1]. In laser-satellite communication systems, uplink transmissions are particularly vulnerable to significant performance degradation caused by atmospheric turbulence [2]. Although both uplink and downlink are influenced by turbulence, the uplink is more severely affected due to increased beam distortion and pointing errors. This is because the optical signal encounters the turbulent atmosphere immediately after it leaves the transmitter. Thus, the turbulence effects play a critical role in uplink communication. Fortunately, positioning the ground station at a higher altitude can help to reduce the effects of turbulence to some extent [3].

The atmospheric turbulence results from fluctuations in the refractive index over space and time, producing eddies of various sizes. These eddies, acting like randomly varying lenses, range from the inner-to-outer scale of turbulence, distorting the optical wavefront and impairing the beam's propagation characteristics, causing beam spread, beam wander, and scintillation [4]. To mitigate the influence of atmospheric turbulence on wave propagation, this study investigates mitigation techniques such as beam shaping and spatial diversity methods. Beam shaping is an efficient technique for controlling the spatial profile of a laser beam, specifically its intensity or phase, to enhance the propagation performance. This approach helps to mitigate the effects of atmospheric turbulence, enables greater power transmission to the receiver, improves signal quality, and extends the communication range. The conversion of Gaussian beams into annular or annular array shapes can be realized through optical components, including axicon lenses, annular apertures, phase plates, diffractive optical elements, holograms, and cylindrical lenses [5], [6], [7]. In addition, using multiple laser sources at the transmitter, positioned at distances greater than the atmospheric coherence length or turbulence correlation width, provides spatial diversity, increasing the transmitted power and reducing the impact of atmospheric turbulence on the optical beam [8], [9], [10]. Adaptive optics offers an alternative solution for turbulence mitigation in uplink laser communications [11], [12]. While this method improves performance, it depends on accurate atmospheric turbulence data and requires costly implementation. Our study instead focuses on passive mitigation approaches.

Vetelino and Andrews [13] analyzed the propagation of an annular beam through horizontal atmospheric turbulence. They modeled the annular beam as the difference of two collimated Gaussian beams having different beam waist sizes. They derived expressions for the intensity and scintillation index, showing that the annular beam exhibits a lower scintillation index than a standard Gaussian beam. Vetelino and Morgan [14] also examined the intensity profile and beam spot size of higher order annular beams propagating through turbulent conditions. Their findings revealed that increasing turbulence strength causes the central dark region of annular beams to gradually fill in. In addition, they observed that

Received 14 July 2025; revised 20 November 2025; accepted 21 November 2025. Date of publication 8 December 2025; date of current version 13 February 2026. This work was supported in part by Dutch Research Council (NWO) through the Project DAILSCOM: Atmospheric Turbulence Informed Machine Learning for Laser Satellite Communications, Open Technology Program 2023-2, under Grant 20617. *(Corresponding author: Muhsin Caner Gökçe.)*

Muhsin Caner Gökçe is with the Department of Geoscience and Remote Sensing, Delft University of Technology, 2628 CN Delft, The Netherlands, and also with the Department of Electrical and Electronics Engineering, TED University, Çankaya, 06420 Ankara, Türkiye (e-mail: m.c.gokce@tudelft.nl).

Rudolf Saathof is with the Department of Space Systems Engineering, Delft University of Technology, 2629 HS Delft, The Netherlands (e-mail: r.saathof@tudelft.nl).

Digital Object Identifier 10.1109/TAP.2025.3639155

higher order modes demonstrate greater resilience to turbulence effects compared to their lower order counterparts. In a separate study, Xiao and Voelz [15] employed wave optics simulations to study annular beam intensity and scintillation index in turbulence, validating their findings against theoretical models.

Two key studies have examined the propagation properties of partially coherent decentered annular beams along inclined paths. Dou et al. [16] analytically determined peak intensity positions by identifying critical points in the intensity distribution function. Building on this foundation, Li and Ji [17] further quantified propagation parameters, including beamwidth, skewness, and kurtosis for these beams in non-Kolmogorov turbulent media. In addition, two further significant studies have investigated the propagation behavior of annular beams [18], [19]. The first study analyzed the scintillation properties of annular beams propagating through the atmospheric turbulence along a slanted path and compared them with those of flat-topped beams [18]. The second study focused on the scintillation characteristics of annular beams in both downlink and uplink scenarios, revealing that the scintillation index is higher for the uplink than for the downlink [19]. Scintillation analysis for annular beam propagation has also been conducted under both non-Kolmogorov weak turbulence conditions [20] and Kolmogorov turbulence environments [21].

The propagation characteristics of annular beams have been explored from several perspectives in the literature. Gercekcioglu [22] analyzed the bit error rate (BER) performance of annular beams for low-Earth orbit (LEO) and geostationary (GEO) satellite communication links under weak atmospheric turbulence, and later extended this work to evaluate communication between an aerial vehicle and a satellite under strong turbulence conditions [23]. Beam wander effects were examined in [24], while the beam spot size and the received power of high-order annular beams were investigated in [25] and [26], respectively. In addition, Zhang et al. [27] studied the self-focusing behavior of annular laser beams propagating through the atmosphere to enhance the efficiency of high-energy laser transmission from space to ground. The propagation of spatially diverted beams in turbulent atmosphere has also been reported in the current literature [28], [29], [30].

The literature further indicates that superior performance enhancements are attainable through the integration of multiple turbulence mitigation techniques. This is effectively illustrated in the work of Elsayed [31], where the joint application of orbital angular momentum, spatial diversity, dense wavelength division multiplexing, and advanced modulation formats resulted in improved performance for free-space optical communication systems. Furthermore, Sayan et al. [32], [33] investigated the scintillation index of Hermite–Gaussian and multimode laser beams in the context of vertical laser-satellite communication links. The scintillation index of a spherical wave for both downlink and uplink under non-Kolmogorov turbulence at large zenith angles has been reported in [34] and [35]. The impact of atmospheric turbulence on the wandering of a Gaussian beam in an uplink scenario has been investigated, comparing both Kolmogorov and non-Kolmogorov models [36].

In this article, we analytically derive mathematical models based on the Huygens–Fresnel principle to study key optical parameters, including receiver intensity, kurtosis parameter, effective beam spot radius, Strehl ratio, beam wander, scintillation index, and BER for an annular beam array propagating in uplink laser-satellite communications. The analysis allows the annular beam array to be simplified into special cases, such as a Gaussian beam array, a single annular beam, or a single Gaussian beam, enabling a comparative evaluation of their propagation performance through these optical metrics. The developed models account for beam diffraction, atmospheric turbulence, transmit diversity, and beam shaping. In addition, numerical results are provided to validate our derived models. As far as we know, no existing studies have examined the propagation characteristics of annular beam arrays in uplink laser-satellite communications. This article will serve as the foundation for an optical communication system that utilizes beam shaping and spatial diversity, designed to function in both weak and strong atmospheric turbulence conditions.

The structure of this article is organized as follows. Section II introduces the proposed lasers and the laser communication system model, along with the formulation of its propagation characteristics. Section III presents the numerical results, and Section IV concludes this article.

II. Formulation

A. System Model

We consider an optical system model for ground-to-satellite uplink communication, where the transmitter consists of multiple annular laser sources. These sources are equally spaced on a ring with a radius of r_0. The optical field distribution of the annular beam array at the transmitter is obtained with the aid of the expression in [4]

$$\begin{aligned} u(\mathbf{s}) &= \sum_{n=1}^{N} A_1 \exp\left\{-\frac{1}{2\alpha_{s1}^2}\left[s_x^2+s_y^2 \right.\right. \\ &\qquad \left.\left. -2r_0\left(s_x\cos\theta_n + s_y\sin\theta_n - 0.5r_0\right)\right]\right\} \\ &\quad - A_2 \exp\left\{-\frac{1}{2\alpha_{s2}^2}\left[s_x^2+s_y^2 \right.\right. \\ &\qquad \left.\left. -2r_0\left(s_x\cos\theta_n + s_y\sin\theta_n - 0.5r_0\right)\right]\right\} \\ &= \sum_{n=1}^{N}\sum_{n1=1}^{2} A_{n1} \exp\left\{-\frac{1}{2\alpha_{sn1}^2}\left[s_x^2+s_y^2 \right.\right. \\ &\qquad \left.\left. -2r_0\left(s_x\cos\theta_n + s_y\sin\theta_n - \frac{r_0}{2}\right)\right]\right\} \end{aligned} \tag{1}$$

where the coordinates $\mathbf{s} = (s_x, s_y)$ define the transmitter spatial plane and N is the number of annular beams. A_1 is the field amplitude of the outer beam (primary) in V/m, with α_{s1} as its source size. r_0 is the ring radius, $\theta_n = 2\pi(n-1)/N$, A_2 is the field amplitude of the inner beam (secondary) in V/m, and α_{s2} is the source size of the inner beam, A_{n1} can be either A_1 or

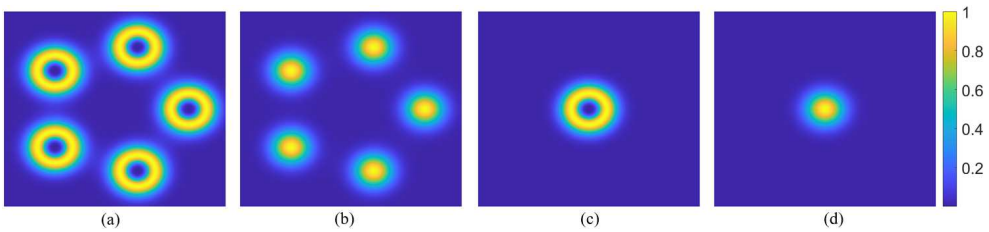

Fig. 1. Normalized intensity distribution of the proposed source model. (a) Annular beam array with $N = 5$. (b) Gaussian beam array with $N = 5$ and $A_2 = 0$. (c) Single annular beam with $N = 1$ and $r_0 = 0$. (d) Single Gaussian beam with $N = 1$, $A_2 = 0$, and $r_0 = 0$. Equal laser source sizes are used here for demonstration purposes.

$-A_2$, and α_{sn1} can be either α_{s1} or α_{s2}. In (1), the annular beam field is created by subtracting two Gaussian beams that have different source sizes. In addition, the amplitudes of the Gaussian beams can be adjusted to produce various beam shapes. It should be noted that our annular beam array model can be simplified to a Gaussian beam array by setting the secondary field amplitude $A_2 = 0$. By choosing the ring radius $r_0 = 0$ and $N = 1$, it can also be reduced to a single annular beam. Furthermore, the model can be reduced to a single Gaussian beam by setting $r_0 = 0$, $N = 1$, and $A_2 = 0$. The normalized intensity distribution of our model at the transmitter is shown as $u(\mathbf{s})\,u^*(\mathbf{s})$ in Fig. 1.

The proposed laser source model is used at the ground-based transmitter in a laser-satellite communication system. The laser beam propagates through the atmospheric turbulence along a slant path and reaches the LEO satellite plane. During propagation, turbulence cells distort the laser wavefront, causing the light to deviate from its initial direction and leading to the wavefront deformation. This deformation, in turn, alters key optical properties of the beam, such as beam spread, wander, and scintillation. The turbulence in the boundary layer of the atmosphere (0–2 km), also known as the surface layer, is the most influential for optical wave propagation, where strong winds, temperature differences i.e., thermal gradients, cause wavefront distortions that can affect the quality of communication. The layer between 2 and 20 km contributes to beam wander due to higher wind speeds and jet streams. Above 20 km, turbulence has little effect on the optical beam, though diffraction continues until the beam reaches the satellite plane. The model of the uplink optical communication system is illustrated in Fig. 2.

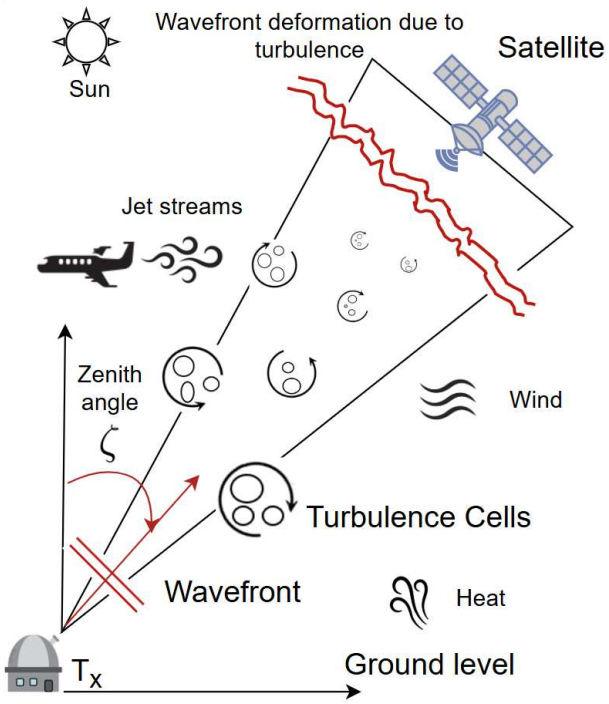

Fig. 2. Ground-to-satellite uplink laser communication system model.

B. Huygens–Fresnel Principle

The optical field at the receiver plane can be described using the Huygens–Fresnel principle as follows [4]:

$$u(\mathbf{p}, L) = \frac{k \exp(ikL)}{2\pi i L} \int_{-\infty}^{\infty}\int_{-\infty}^{\infty} u(\mathbf{s}) \times \exp\left\{\frac{ik}{2L}\left[(s_x - p_x)^2 + (s_y - p_y)^2\right]\right\} \times \exp\left[\psi(\mathbf{s}, \mathbf{p})\right] \mathrm{d}s_x\, \mathrm{d}s_y \quad (2)$$

where $\mathbf{p} = (p_x, p_y)$ represents the spatial coordinates of the receiver plane, L is the propagation distance, $k = 2\pi/\lambda$ is the wavenumber, λ is the wavelength, $i = \sqrt{-1}$ denotes the imaginary unit, and $\psi(\cdot)$ is the random part of the complex phase of a spherical wave representing the atmospheric turbulence.

C. Receiver Optical Intensity

The receiver optical intensity of an annular beam array by the Huygens–Fresnel principle can be found as follows [37]:

$$\begin{aligned}\langle I(\mathbf{p}, L)\rangle &= \langle u(\mathbf{p}, L)\, u^*(\mathbf{p}, L)\rangle \\ &= \frac{1}{(\lambda L)^2}\int_{-\infty}^{\infty}\int_{-\infty}^{\infty}\int_{-\infty}^{\infty}\int_{-\infty}^{\infty} u(\mathbf{s}_1)\, u^*(\mathbf{s}_2) \\ &\quad \times \exp\left[\frac{jk}{2L}\left(|\mathbf{s}_1 - \mathbf{p}|^2 - |\mathbf{s}_2 - \mathbf{p}|^2\right)\right] \\ &\quad \times \left\langle \exp\left[\psi(\mathbf{s}_1, \mathbf{p})\right] \exp\left[\psi^*(\mathbf{s}_2, \mathbf{p})\right]\right\rangle \mathrm{d}^2\mathbf{s}_1\, \mathrm{d}^2\mathbf{s}_2 \quad (3)\end{aligned}$$

where the ensemble average term in the second line of (4) is given by [37]

$$\left\langle \exp\left[\psi(s_1, \mathbf{p})\right] \exp\left[\psi^*(s_2, \mathbf{p})\right]\right\rangle = \exp\left[-\frac{1}{2} D(\mathbf{s}_1, \mathbf{s}_2)\right] \quad (4)$$

where $D(\mathbf{s}_1, \mathbf{s}_2)$ is the wave structure function defined by the transverse coordinates of the source, and the approximate form is defined by [37]

$$D(\mathbf{s}_1, \mathbf{s}_2) = \frac{2}{\rho_0^2}(\mathbf{s}_1 - \mathbf{s}_2)^2 \tag{5}$$

where ρ_0 represents the coherence length of a spherical wave traveling along a slant atmospheric path. Substituting (1) into (3) and evaluating the integral using the formula from [38, eq. (3.323.2)], we obtain the analytical expression for the optical intensity at the receiver plane as follows:

$$\begin{aligned}\langle I(\mathbf{p}, z = L)\rangle = &\left(\frac{1}{\lambda L}\right)^2 \pi^2 \sum_{n=1}^{N}\sum_{m=1}^{M}\sum_{n1=1}^{2}\sum_{m1=1}^{2}\frac{A_{n1}A_{m1}}{t_1^2 t_2^2}\\ &\times \exp\left[-\frac{r_0^2}{2}\left(\frac{1}{\alpha_{sn1}^2}+\frac{1}{\alpha_{sm1}^2}\right)+\frac{r_0^2}{4t_2^2\alpha_{sm1}^4}\right]\\ &\times \exp\left[-\frac{k^2}{4t_2^2L^2}\left(p_x^2+p_y^2\right)\right]\\ &\times \exp\left[\frac{r_0 ik}{2t_2^2\alpha_{sm1}^2 L}\left(p_x\cos\theta_m + p_y\sin\theta_m\right)\right]\\ &\times \exp\left[\frac{1}{4t_1^2}\left(w_{1x}^2+w_{1y}^2\right)\right]\end{aligned} \tag{6}$$

where

$$\begin{aligned} t_1^2 &= \frac{1}{2\alpha_{sn1}^2} - \frac{ik}{2L} + \frac{1}{\rho_0^2} - \frac{1}{t_2^2\rho_0^4}\\ t_2^2 &= \frac{1}{2\alpha_{sm1}^2} + \frac{ik}{2L} + \frac{1}{\rho_0^2}\\ w_{1x} &= \frac{r_0\cos\theta_n}{\alpha_{sn1}^2} - \frac{ikp_x}{L} + \frac{r_0\cos\theta_m}{t_2^2\alpha_{sm1}^2\rho_0^2} + \frac{ikp_x}{t_2^2 L\rho_0^2}\\ w_{1y} &= \frac{r_0\sin\theta_n}{\alpha_{sn1}^2} - \frac{ikp_y}{L} + \frac{r_0\sin\theta_m}{t_2^2\alpha_{sm1}^2\rho_0^2} + \frac{ikp_y}{t_2^2 L\rho_0^2}. \end{aligned}$$

D. Coherence Length Based on the Hufnagel–Valley (H–V) Method

Vertical profile of the structure constant according to H–V is given by [39], [40]

$$\begin{aligned} C_n^2(h) = &\,0.00594\left(\frac{w}{27}\right)^2\left(10^{-5}h\right)^{10}\exp\left(-\frac{h}{1000}\right)\\ &+ 2.7\times 10^{-16}\exp\left(-\frac{h}{1500}\right)\\ &+ C_{n0}^2\exp\left(-\frac{h}{100}\right)\end{aligned} \tag{7}$$

where $C_n^2(h)$ is the structure constant which depends on vertical height h, w represents the root mean square (rms) wind speed, measured in m/s, and C_{n0}^2 denotes the structure constant at ground level in $\mathrm{m}^{-2/3}$. The relationship between the vertical and slant paths is given by $h = \eta\cos(\zeta)$, where ζ is the zenith angle and η is the distance parameter along the propagation axis. Inserting this relation into (7), we can obtain the slant path structure constant.

Finally, the coherence length of the spherical wave passing through the slant atmospheric turbulence is expressed by [41], [42]

$$\rho_0 = \left[1.457k^2\int_0^L C_n^2(\eta)\,d\eta\right]^{-3/5}. \tag{8}$$

By substituting (8) into the integral in (8) and performing the integration over the entire propagation path, we obtain (9)

$$\begin{aligned} &\int_0^L C_n^2(\eta)\,d\eta\\ &= 0.00594\left(\frac{w}{27}\right)^2\left(10^{-5}\cos\zeta\right)^{10}\int_0^L \eta^{10}\exp\left(-\frac{\eta\cos\zeta}{1000}\right)d\eta\\ &\quad + 2.7\times 10^{-16}\int_0^L \exp\left(-\frac{\eta\cos\zeta}{1500}\right)d\eta\\ &\quad + C_{n0}^2\int_0^L \exp\left(-\frac{\eta\cos\zeta}{100}\right)d\eta\\ &= 0.00594\left(\frac{w}{27}\right)^2 10^{-50}\cos^9\zeta\\ &\quad\left[\frac{10!\cdot 10^{33}}{\cos^{10}\zeta} - \exp\left(-\frac{L\cos\zeta}{1000}\right)\sum_{m=0}^{10}\frac{10!}{m!}\cdot\frac{L^m\cdot 10^{33-3m}}{\cos^{10-m}\zeta}\right]\\ &\quad + \frac{4050\times 10^{-16}}{\cos\zeta}\left[1-\exp\left(-\frac{L\cos\zeta}{1500}\right)\right]\\ &\quad + \frac{100C_{n0}^2}{\cos\zeta}\left[1-\exp\left(-\frac{L\cos\zeta}{100}\right)\right]. \end{aligned} \tag{9}$$

It is important to highlight that (9) represents the corrected version, derived from [42, eq. (10)], which contains a typographical error. The corrected formulation is given in (9) in this article. We have added $\cos(\zeta)$ to the denominator of both the second and third terms in [42, eq. (10)]. It is also important to note that a closed-form expression is required to numerically evaluate the beam wander given in (19); this necessity motivated the derivation of (9) in this study.

E. Kurtosis Parameter

In this article, the kurtosis parameter is employed to analyze the behavior of optical beam propagation in atmospheric turbulence. It provides valuable insight into how the beam's shape deviates from a Gaussian distribution. A Gaussian beam maintains a kurtosis value of 3, signifying a mesokurtic distribution. When the kurtosis exceeds 3 (indicating a leptokurtic distribution), the distribution of the beam's tails becomes narrower, resulting in a sharper peak and intensity suppression. On the other hand, when the kurtosis falls below 3 (indicating a platykurtic distribution), the tails broaden, leading to an increased spatial spread of the beam compared with a Gaussian distribution.

The kurtosis parameter of the annular beam array along the p_x direction is expressed as follows [43], [44]:

$$K_x = \frac{\langle p_x^4\rangle}{\langle p_x^2\rangle^2} \tag{10}$$

where $\langle p_x^4 \rangle$ is the fourth-order intensity moment and $\langle p_x^2 \rangle$ is the second-order intensity moment and $\langle p_x^r \rangle$ is given by

$$\left\langle p_x^r \right\rangle = \frac{\int_{-\infty}^{\infty}\int_{-\infty}^{\infty} p_x^r \langle I(\mathbf{p}, z=L)\rangle \, dp_x dp_y}{\int_{-\infty}^{\infty}\int_{-\infty}^{\infty} \langle I(\mathbf{p}, z=L)\rangle \, dp_x dp_y}, \quad r = 2, 4 \tag{11}$$

where the denominator represents the total optical power at the receiver plane. It is essential to highlight that K_y is obtained by substituting the coordinate parameter p_x of the receiving plane with p_y, while K_{xy} is determined as $K_{xy} = \sqrt{K_x K_y}$. By inserting the intensity expression from (6) into the numerator of (11) and solving the integral, we obtain

$$\begin{aligned}
&\int_{-\infty}^{\infty}\int_{-\infty}^{\infty} p_x^r \langle I(\mathbf{p}, z=L)\rangle \, dp_x dp_y \\
&= \left(\frac{1}{\lambda L}\right)^2 \pi^3 \sum_{n=1}^{N}\sum_{m=1}^{M}\sum_{n1=1}^{2}\sum_{m1=1}^{2} A_{n1}A_{m1}\frac{1}{t_1^2 t_2^2} \\
&\quad \times \exp\left[-\frac{r_0^2}{2}\left(\frac{1}{\alpha_{sn1}^2}+\frac{1}{\alpha_{sm1}^2}\right)+\frac{r_0^2}{4t_2^2\alpha_{sm1}^4}\right] \\
&\quad \times \exp\left[\frac{1}{4t_1^2}\left(\frac{r_0\cos\theta_n}{\alpha_{sn1}^2}+\frac{r_0\cos\theta_m}{t_2^2\alpha_{sm1}^2\rho_0^2}\right)^2\right] \\
&\quad \times \exp\left[\frac{1}{4t_1^2}\left(\frac{r_0\sin\theta_n}{\alpha_{sn1}^2}+\frac{r_0\sin\theta_m}{t_2^2\alpha_{sm1}^2\rho_0^2}\right)^2\right] \\
&\quad \times \exp\left(\frac{C_x^2+C_y^2}{4C}\right) C^{-\frac{2+r}{2}} (2i)^{-r} H_r\left(\frac{iC_x}{2\sqrt{C}}\right)
\end{aligned} \tag{12}$$

where

$$C = \frac{k^2}{4t_2^2L^2} + \frac{1}{4t_1^2}\frac{k^2}{L^2}\left(1-\frac{1}{t_2^2\rho_0^2}\right)^2 \tag{13}$$

$$\begin{aligned}
C_x = &\frac{r_0 ik}{2t_2^2\alpha_{sm1}^2 L}\cos\theta_m - \frac{1}{2t_1^2}\left(\frac{r_0\cos\theta_n}{\alpha_{sn1}^2}+\frac{r_0\cos\theta_m}{t_2^2\alpha_{sm1}^2\rho_0^2}\right) \\
&\times \frac{ik}{L}\left(1-\frac{1}{t_2^2\rho_0^2}\right)
\end{aligned} \tag{14}$$

$$\begin{aligned}
C_y = &\frac{r_0 ik}{2t_2^2\alpha_{sm1}^2 L}\sin\theta_m - \frac{1}{2t_1^2}\left(\frac{r_0\sin\theta_n}{\alpha_{sn1}^2}+\frac{r_0\sin\theta_m}{t_2^2\alpha_{sm1}^2\rho_0^2}\right) \\
&\times \frac{ik}{L}\left(1-\frac{1}{t_2^2\rho_0^2}\right).
\end{aligned} \tag{15}$$

It is worth noting that the total power at the receiver plane, given by the denominator of (11), can be obtained from (12) by setting $r = 0$ in the equation. In addition, to calculate the numerator of (11), we utilized the following integral formula we derived:

$$\int_{-\infty}^{\infty} x^n e^{-px^2+qx} dx = e^{\frac{q^2}{4p}} \sqrt{\pi}\, p^{-\frac{1+n}{2}} (2i)^{-n} H_n\left(\frac{iq}{2\sqrt{p}}\right) \tag{16}$$

where $H_n(.)$ denotes the Hermite polynomial of order n. One may also apply the formula from [38, eq. (3.462.2)] to evaluate the integral given in (12) without involving the Hermite polynomial.

F. Effective Beam Spot Radius

Determining the footprint of a propagating beam for uplink communication is crucial, as it provides an estimate of the optical power received at the detector and aids in beam alignment. The mean squared beamwidth (σ_x^2) of the annular beam array is given by [4], [44]

$$\sigma_x^2 = \frac{2\int_{-\infty}^{\infty}\int_{-\infty}^{\infty} p_x^2 \langle I(\mathbf{p}, z=L)\rangle \, dp_x \, dp_y}{\int_{-\infty}^{\infty}\int_{-\infty}^{\infty} \langle I(\mathbf{p}, z=L)\rangle \, dp_x \, dp_y} = 2\left\langle p_x^2 \right\rangle \tag{17}$$

where σ_x represents the effective beam spot radius along the p_x axis. Here, we note that the beam spot radius σ_x is given by the square root of twice the second-order intensity moment, expressed as $\sqrt{2\langle p_x^2 \rangle}$, where the analytical solution can be derived from the expression in (12).

G. Strehl Ratio

The Strehl ratio is a measure of the quality of an optical beam used in laser-satellite communications. It is defined as the ratio of the maximum optical intensity in the presence of turbulence to the maximum intensity in a turbulence-free environment. A Strehl ratio of 1 indicates that there is no impact from turbulence on the optical beam, while a ratio approaching 0 suggests that turbulence has significantly distorted the beam, leading to substantial intensity attenuation due to atmospheric turbulence. In a laser-satellite communication system, an optical beam with a higher Strehl ratio is better for enhancing the quality of communication. In this study, we will evaluate and compare the Strehl ratios of the annular beam array, laser beam array, single annular beam, and single Gaussian beam. Rather than using the standard definition of the Strehl ratio, we will determine it based on the ratio of the square of beam size in a turbulence-free environment to the square of beam size under turbulent conditions, given by [11], [45]

$$\text{Strehl Ratio} \cong \frac{{\sigma_{x\_fs}}^2}{{\sigma_x}^2}. \tag{18}$$

Here, σ_{x_fs} denotes the beam spot radius along the p_x axis in the absence of turbulence. Note that during propagation, the annular beam array displays multiple maxima and minima. Identifying the maxima requires further mathematical expressions, which are not discussed in this article. Instead, we adopt the square of beam spot radius ratio definition from (18) for simplicity, avoiding complex mathematical derivations to determine the beam's maximum point.

H. Beam Wander

The analytical expression for beam wander under varying turbulence conditions, including weak, moderate, and strong turbulence, is given as follows [46], [47]:

$$\begin{aligned}
\left\langle r_c^2 \right\rangle = &4\pi k^2 \sigma_{x_fs}^2 \int_0^L \int_0^\infty \kappa \Phi_n(\kappa, z) \exp\left[-\kappa^2 \sigma_x^2(z)\right] \\
&\times \left\{1 - \exp\left[-\frac{2L^2\kappa^2(1-z/L)^2}{k^2\sigma_{x_fs}^2}\right]\right\} d\kappa \, dz
\end{aligned} \tag{19}$$

where κ denotes the spatial frequency and $\Phi_n(\kappa)$ represents the power spectrum of atmospheric turbulence, which is considered to follow the Kolmogorov spectrum in this study, i.e.,

$$\Phi_n(\kappa, z) = 0.033\, C_n^2(z)\, \kappa^{-11/3}. \tag{20}$$

Based on the Kolmogorov spectrum in (20), the slant path structure constant in (9), and the analytically derived beam spot size in (17), the beam wander for the slant path is numerically evaluated and presented in the Section III.

I. Scintillation Index

Scintillation, also referred to as signal fading, is an essential parameter in optical communication systems that degrades link performance operating in atmospheric turbulence. It represents fluctuations in the received signal intensity and is measured using the scintillation index. Under weak turbulence conditions, and using the Rytov method, the scintillation index for a laser beam propagating a distance L from a ground-based transmitter to a satellite can be expressed as follows [48], [49]:

$$\begin{aligned} m^2(\mathbf{p}, L) = 4\pi \int_0^L \int_0^\infty \int_0^{2\pi} d\eta\, \kappa\, d\kappa\, d\phi_\kappa\, \Phi(\kappa, \eta) \\ \times \left\{ H(p_x, p_y, \kappa, \phi_\kappa, \eta)\, H^*(p_x, p_y, \kappa, \phi_\kappa, \eta) \right. \\ \left. + \mathrm{Re}\left[H(p_x, p_y, \kappa, \phi_\kappa, \eta)\, H(p_x, p_y, -\kappa, \phi_\kappa, \eta) \right] \right\} \end{aligned} \tag{21}$$

where ϕ_κ denotes the angular orientation of spatial frequency, Re denotes the real part, and $H(\cdot)$ denotes the fluctuation of the complex amplitude induced by turbulence, relative to the turbulence-free field, and is expressed through the following integral:

$$\begin{aligned} H(\mathbf{p}, \kappa, \phi_\kappa, \eta) = \frac{k^2 \exp\left[ik(L-\eta)\right]}{2\pi(L-\eta)\, u_r(\mathbf{p}, z=L)} \\ \times \exp\left[\frac{ik\mathbf{p}^2}{2(L-\eta)}\right] \int_{-\infty}^{\infty}\int_{-\infty}^{\infty} dp_{1x} dp_{1y} u_r(p_{1x}, p_{1y}, z=\eta) \\ \times \exp\left\{ i\kappa\left[p_{1x}\cos(\phi_\kappa) + p_{1y}\sin(\phi_\kappa) \right] \right\} \\ \times \exp\left[\frac{ik}{2(L-\eta)} \left(p_{1x}^2 + p_{1y}^2 - 2p_x p_{1x} - 2p_y p_{1y} \right) \right] \end{aligned} \tag{22}$$

where $u_r(p_{1x}, p_{1y}, z = \eta)$ is the turbulence-free field. By employing (1) and applying the Huygens–Fresnel integral from (2) with the turbulence term excluded, the receiver optical field of the annular beam array under turbulence-free conditions is expressed as follows:

$$\begin{aligned} u_r(\mathbf{p}_1, L) = \frac{k\exp(ikL)}{2\pi iL} \sum_{n=1}^{N}\sum_{n1=1}^{2} A_{n1} \frac{\pi}{t_{1fs}^2} \\ \times \exp\left[-\frac{r_0^2}{2\alpha_{sn1}^2} + \frac{r_0^2}{4t_{1fs}^2\alpha_{sn1}^4} \right] \\ \times \exp\left[-p_{1x}^2 \left(\frac{k^2}{4t_{1fs}^2 L^2} - \frac{ik}{2L} \right) - p_{1x} \frac{ikr_0\cos\theta_n}{2t_{1fs}^2 L\alpha_{sn1}^2} \right] \\ \times \exp\left[-p_{1y}^2 \left(\frac{k^2}{4t_{1fs}^2 L^2} - \frac{ik}{2L} \right) - p_{1y} \frac{ikr_0\sin\theta_n}{2t_{1fs}^2 L\alpha_{sn1}^2} \right] \end{aligned} \tag{23}$$

where $t_{1fs}^2 = 1/(2\alpha_{sn1}^2) - ik/(2L)$. Substituting (22) into (21) and evaluating the integral over p_{1x} and p_{1y}, the closed-form expression for $H(\cdot)$ is obtained as follows:

$$\begin{aligned} H(p_x, p_y, \kappa, \phi_\kappa, \eta) = -i \frac{k^3 \exp(ikL)}{4\pi^2\eta(L-\eta)\, u(\mathbf{p}, z=L)} \\ \times \exp\left[\frac{ik\left(p_x^2 + p_y^2\right)}{2(L-\eta)} \right] \sum_{n=1}^{N}\sum_{n1=1}^{2} A_{n1} \frac{\pi^2}{t_{1fs}^2 t_H^2} \\ \times \exp\left(-\frac{r_0^2}{2\alpha_{sn1}^2} + \frac{r_0^2}{4t_{1fs}^2\alpha_{sn1}^4} + \frac{w_{Hx}^2 + w_{Hy}^2}{4t_H^2} \right) \end{aligned} \tag{24}$$

where $t_H^2 = k^2/4t_{1fs}^2\eta^2 - ik/2\eta - ik/2(L-\eta)$, $w_{Hx} = -ikr_0\cos\theta_n/2t_{1fs}^2\eta\alpha_{sn1}^2 + i\kappa\cos(\phi_\kappa) - ik/(L-\eta)p_x$, and $w_{Hy} = -ikr_0\sin\theta_n/2t_{1fs}^2\eta\alpha_{sn1}^2 + i\kappa\sin(\phi_\kappa) - ik/(L-\eta)p_y$. Substituting (24) and the von Kármán spectrum into (21) and evaluating the integral over ϕ_κ and κ yields the solution

$$\begin{aligned} m^2(p, \phi_r, L) = \frac{0.033\pi^2 k^6}{4|u(0, z=L)|^2} \\ \times \sum_{n=1}^{N}\sum_{n1=1}^{2}\sum_{m=1}^{M}\sum_{m1=1}^{2}\sum_{\Omega=0}^{\infty} \frac{\kappa_0^{2\Omega-5/3} A_{n1}A_{m1}}{\Omega!} \\ \times \int_0^L d\eta C_n^2(\eta) \frac{1}{t_{1fs}^2 t_H^2 \left(t_{1fsm}^2\right)^* \left(t_{Hm}^2\right)^* (L-\eta)^2\eta^2} \\ \times \exp\left[-\frac{r_0^2}{2\alpha_{sn1}^2} + \frac{r_0^2}{4t_{1fs}^2\alpha_{sn1}^4} \left(1 - \frac{k^2}{4t_H^2 t_{1fs}^2\eta^2} \right) \right] \\ \times \exp\left[-\frac{r_0^2}{2\alpha_{sm1}^2} + \frac{r_0^2}{4\left(t_{1fsm}^2\right)^*\alpha_{sm1}^4} \right. \\ \left. \times \left(1 - \frac{k^2}{4\left(t_{Hm}^2\right)^*\left(t_{1fsm}^2\right)^*\eta^2} \right) \right] \\ \times \left(\frac{\beta^2}{4} \right)^{\Omega} U\left(\Omega+1, \frac{6\Omega+1}{6}, \delta\kappa_0^2 \right) \\ - \mathrm{Re}\left\{ 0.033 \frac{\pi^2 k^6 \exp(i2kL)}{4u(0, z=L)^2} \right. \\ \times \sum_{n=1}^{N}\sum_{n1=1}^{2}\sum_{m=1}^{M}\sum_{m1=1}^{2}\sum_{\Omega=0}^{\infty} \frac{\kappa_0^{2\Omega-5/3} A_{n1}A_{m1}}{\Omega!} \\ \times \int_0^L d\eta C_n^2(\eta) \frac{1}{t_{1fs}^2 t_H^2 t_{1fsm}^2 t_{Hm}^2 (L-\eta)^2\eta^2} \\ \times \exp\left[-\frac{r_0^2}{2\alpha_{sn1}^2} + \frac{r_0^2}{4t_{1fs}^2\alpha_{sn1}^4} \left(1 - \frac{k^2}{4t_H^2 t_{1fs}^2\eta^2} \right) \right] \\ \times \exp\left[-\frac{r_0^2}{2\alpha_{sm1}^2} + \frac{r_0^2}{4t_{1fsm}^2\alpha_{sm1}^4} \left(1 - \frac{k^2}{4t_{Hm}^2 t_{1fsm}^2\eta^2} \right) \right] \\ \left. \times \left(\frac{\beta_2^2}{4} \right)^{\Omega} U\left(\Omega+1, \frac{6\Omega+1}{6}, \delta_2\kappa_0^2 \right) \right\} \end{aligned} \tag{25}$$

where $\kappa_0 = 2\pi/L_0$, and L_0, the outer scale of turbulence, is set to 100 m in this study for numerical calculations, in order to

approach the Kolmogorov regime, $t_{1fsm}^2 = 1/(2\alpha_{sm1}^2) - ik/(2\eta)$, $t_{Hm}^2 = k^2/4t_{1fsm}^2\eta^2 - ik/2\eta - ik/2(L-\eta)$, $U(\cdot)$ is the Tricomi's confluent hypergeometric function, $\delta = 1/4\left[1/t_H^2 + 1/(t_{Hm}^2)^*\right]$, $\delta_2 = 1/4\left(1/t_H^2 + 1/t_{Hm}^2\right)$, $\beta = \sqrt{c_1^2 + c_2^2}$, $\beta_2 = \sqrt{c_3^2 + c_4^2}$, and $c_1 = kr_0\cos\theta_n/4t_H^2t_{1fs}^2\eta\alpha_{sn1}^2 + kr_0\cos\theta_m/4(t_{Hm}^2)^*(t_{1fsm}^2)^*\eta\alpha_{sm1}^2$, $c_2 = kr_0\sin\theta_n/4t_H^2t_{1fs}^2\eta\alpha_{sn1}^2 + kr_0\sin\theta_m/4(t_{Hm}^2)^*(t_{1fsm}^2)^*\eta\alpha_{sm1}^2$, $c_3 = kr_0\cos\theta_n/4t_H^2t_{1fs}^2\eta\alpha_{sn1}^2 - kr_0\cos\theta_m/4t_{Hm}^2t_{1fsm}^2\eta\alpha_{sm1}^2$, and $c_4 = kr_0\sin\theta_n/4t_H^2t_{1fs}^2\eta\alpha_{sn1}^2 - kr_0\sin\theta_m/4t_{Hm}^2t_{1fsm}^2\eta\alpha_{sm1}^2$. Because $\delta_2\kappa_0^2 \ll 1$ in Tricomi's function, an approximation can be applied to accelerate the numerical calculation.

It should be noted that the derived scintillation index m^2 in (25) reduces to the Gaussian-beam scintillation index in the appropriate limiting case. The results in this limit are consistent with those shown in [4, Fig. 12.12] (see the on-axis scintillation index of the tracked beam).

J. Bit Error Rate

The performance of a laser-satellite communication system, influenced by atmospheric scintillation, turbulence-affected intensity, and other system parameters, is quantified using the BER, which serves as the ultimate indicator for system performance. The unconditional BER performance of a laser-satellite communication system employing pulse-position modulation (PPM) is statistically determined and bounded by [9]

$$P_e^M \le \frac{M_o}{2\sqrt{\pi}} \sum_{j=1}^{T} w_j Q\left(\frac{W_n}{W_d}\right) \tag{26}$$

where M_o is the modulation order and $[w_j]_{j=1}^T$ are the weight of the jth-order Hermite polynomials, $Q(x) = 0.5\text{erfc}(x/\sqrt{2})$, where erfc$(\cdot)$ is the complementary error function

$$W_n = \exp\left\{2\sqrt{2}\left[\ln\left(m^2+1\right)\right]^{0.5} x_j - \ln\left(m^2+1\right) + 2\ln\left(\frac{\eta_q\,\lambda\,\langle I(L)\rangle\,T_s}{\hbar c}\right)\right\} \tag{27}$$

$$W_d = F_n W_n^{0.5} + \frac{2\sigma_{Th}^2}{(M_D q)^2} + 2F_n K_{Bg} \tag{28}$$

where m^2 denotes the scintillation index, as given in (25), $[x_j]_{j=1}^T$ are zeros for the jth-order Hermite polynomials, η_q is quantum efficiency of the photodetector, $\langle I(L)\rangle$ is the average intensity, as given in (6), $T_s = T_b\log_2(M)/M$, $T_b = 1/R_b$, R_b being the data bit rate of the laser-satellite communication link, $\hbar$ is Planck's constant, c is the speed of light, $F = 2 + \varsigma M_D$ is the noise factor of the APD, ς is the APD ionization factor, M_D is the average current gain of the APD, $\sigma_{Th}^2 = 2K_BT_eT_s/R_L$ is the equivalent noise count during a PPM slot, K_B is Boltzmann's constant, T_e is the receiver temperature in degrees Kelvin, R_L is the APD load resistance, $q = 1.6\times10^{-19}$ coulombs is the electron charge, and $K_{Bg} = \eta_q\lambda P_{\text{Bg}}T_s/(\hbar c)$ is the average photon count in the PPM slot because of the background power radiation P_{Bg}. For the numerical calculations, we set $P_{\text{Bg}} = 0.1\times I(L)$, where $I(L)$ represents the optical intensity in the absence of turbulence.

Note that PPM encodes information in the timing of pulses and is widely employed in laser-satellite communication due to its superior energy efficiency compared to alternative modulation schemes. Accordingly, it has been adopted in the present study.

TABLE I
SIMULATION PARAMETERS

Symbol	Definition	Value
λ	Wavelength	1550 nm
C_{n0}^2	Ground-level structure constant	1×10^{-14} m$^{-2/3}$
w	Wind speed	21 m/s
ζ	Zenith angle	30°
L	Propagation distance	701 km
α_{s1}	Primary source size	20 cm
α_{s2}	Secondary source size	10 cm
A_1	Primary beam amplitude	1 V/m
A_2	Secondary beam amplitude	1 V/m
r_0	Ring radius	80 cm
N	Number of laser beams	3

III. NUMERICAL RESULTS

A. Numerical Results for the Strehl Ratio, Beam Spot Radius, Kurtosis Parameter, and Beam Wander

This section provides numerical results for the derived formulations of the annular beam array, including the Strehl ratio, beam spot radius, kurtosis parameter, and rms beam wander. Using our mathematical model, we compare the propagation of an array with annular beams to that of Gaussian beams, as well as single annular and single Gaussian beams. For a single laser $N = 1$, the ring radius r_0 is set to $r_0 = 0$, indicating that the laser is positioned on the axis. When the secondary field amplitude vanishes ($A_2 = 0$), the beam profile in (1) converts from an annular beam to a Gaussian beam. For Figs. 3–14, A_1 is set to 1. The propagation characteristic of the Gaussian laser is shown in the figures as a benchmark. All system parameters are set to the values provided in Table I, unless otherwise stated in the figure captions or within the figures.

Fig. 3 demonstrates the intensity distributions of the proposed model at propagation distances of $L = 0$ (at the source), 100, and 701 km for: (a) annular beam array, (b) Gaussian beam array, (c) single annular beam, and (d) single Gaussian beam. The figure illustrates how the intensity profiles evolve with propagation. As the distance increases, the spacing within the annular beam array diminishes, and the annular shape gradually transforms into a Gaussian profile: the central hole disappears, and the annular array resembles a Gaussian array at $L = 100$ km. At the satellite distance ($L = 701$ km), all beam types converge to a Gaussian distribution. At $L = 100$ km, the intensity distribution of the single annular beam resembles a Gaussian profile.

In Fig. 4, we show the Strehl ratio as a function of propagation distance for various beam shapes, including the annular beam array, Gaussian beam array, single annular beam, and single Gaussian beam. It is seen that as the propagation distance increases, the Strehl ratio decreases for all beam shapes. When comparing different beam configurations at a fixed distance, the annular beam array maintains the highest

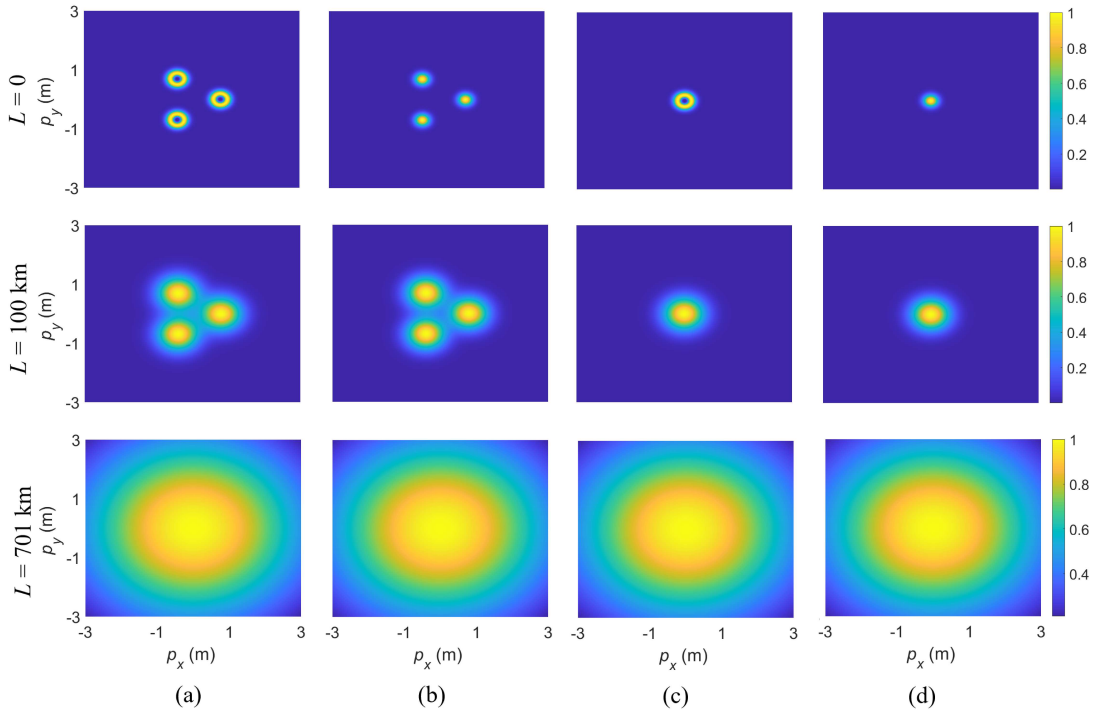

Fig. 3. Intensity distributions of the proposed source model at different propagation distances. (a) Annular array $N = 3$. (b) Gaussian array, $N = 3$ and $A_2 = 0$. (c) Single annular, $N = 1$ and $r_0 = 0$. (d) Single Gaussian, $N = 1$, $A_2 = 0$, and $r_0 = 0$.

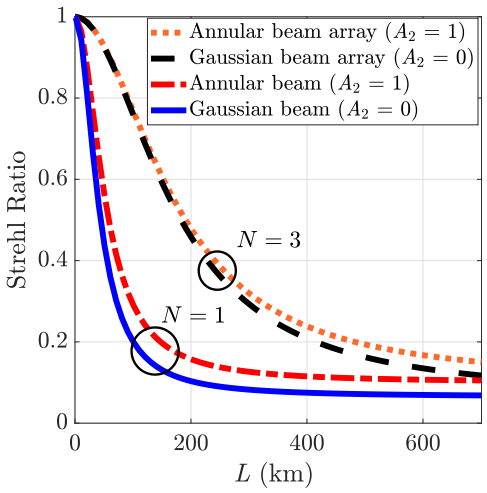

Fig. 4. Strehl ratio versus propagation distance L obtained for various beam shapes.

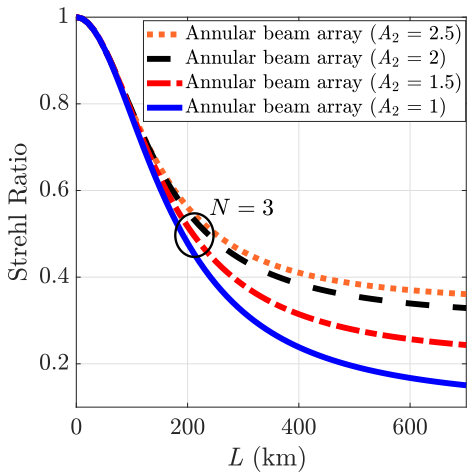

Fig. 5. Strehl ratio of an annular beam array versus propagation distance L obtained for various secondary field amplitudes A_2 (V/m).

Strehl ratio, followed by the Gaussian beam array, the single annular beam, and finally the single Gaussian beam, which exhibits the poorest performance. Similarly, in Fig. 5, we illustrate the dependence of the Strehl ratio on propagation distance for an annular beam array with different secondary field amplitudes A_2. It is noteworthy that a higher secondary field amplitude A_2 leads to an improvement in the Strehl ratio.

Fig. 6 examines the effect of both the number of annular lasers N and the ring radius r_0 on Strehl ratio performance. The results indicate that as the number of annular lasers in the array increases, the Strehl ratio decreases. For a fixed N, increasing the ring radius improves the Strehl ratio. In addition, beyond a certain number of annular lasers, the Strehl ratio reaches a saturation point, which is more pronounced for smaller ring radii. This behavior occurs because fewer annular lasers are needed to completely fill a ring with a smaller radius. Once the ring is fully occupied by annular lasers, further increases in N no longer influence the Strehl ratio performance.

Fig. 7 illustrates the Strehl ratio versus the zenith angle for various beam shapes, including the annular beam array, Gaussian beam array, single annular beam, and single Gaussian beam. As illustrated in the figure, the Strehl ratio decreases with increasing zenith angle. Among different beam types, the annular beam array exhibits the highest Strehl ratio

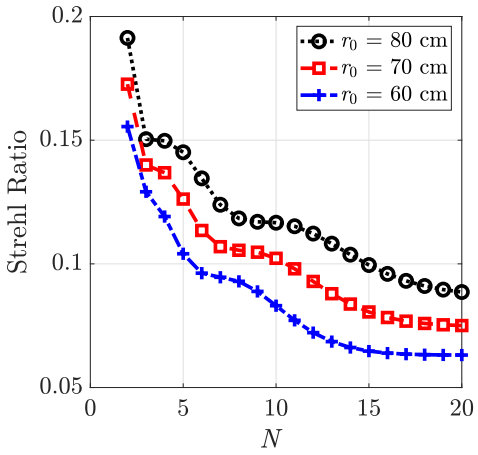

Fig. 6. Strehl ratio of an annular beam array versus number of annular beams N for various ring radii r_0.

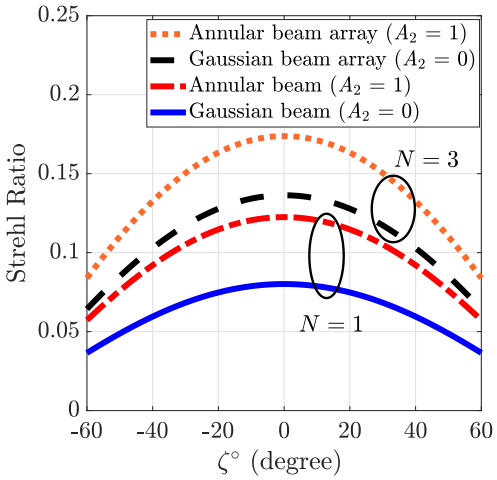

Fig. 7. Strehl ratio versus zenith angle $\zeta°$ for various beam shapes at L = 701 km. The circle enclosing N = 3 illustrates the beam array for both the Gaussian and annular beams, whereas N = 1 corresponds to their single-beam cases.

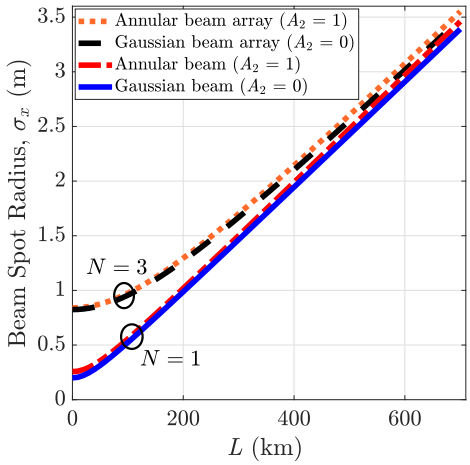

Fig. 8. Effective beam spot radius versus propagation distance L for various beam shapes.

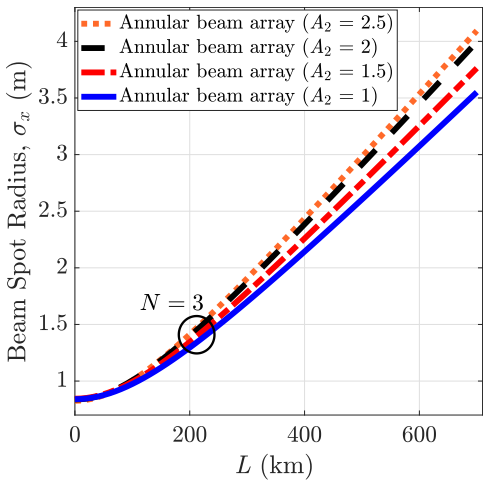

Fig. 9. Effective beam spot radius versus propagation distance L for various secondary field amplitudes A_2 (V/m).

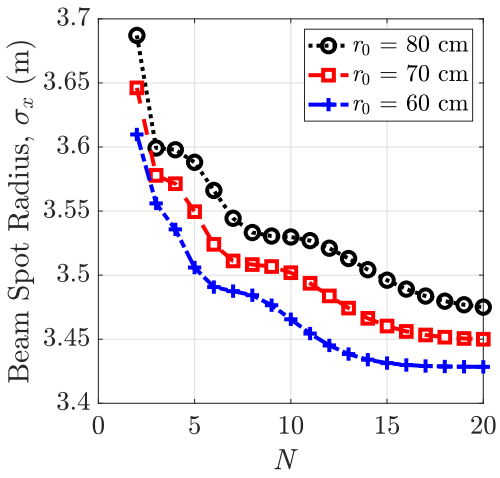

Fig. 10. Effective beam spot radius versus number of annular beams N for various ring radius r_0 values.

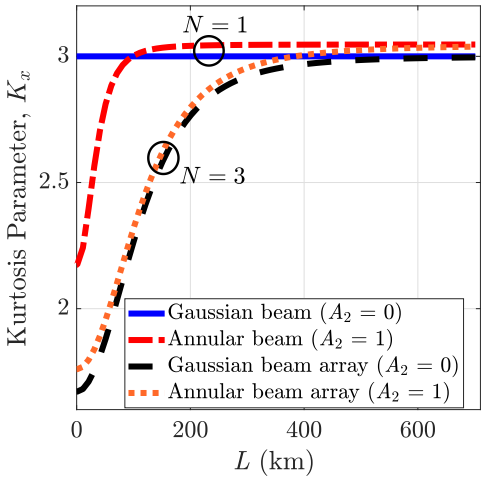

Fig. 11. Kurtosis parameter versus propagation distance L for various beam shapes.

performance. Because the selected inner source size α_{s1} is 20 cm, the resulting Strehl ratio values are quite low. However, for zenith angles between −30° and 30°, the Strehl ratio for an annular beam array with N = 3 remains above 0.15, which is tolerable for laser-satellite communication.

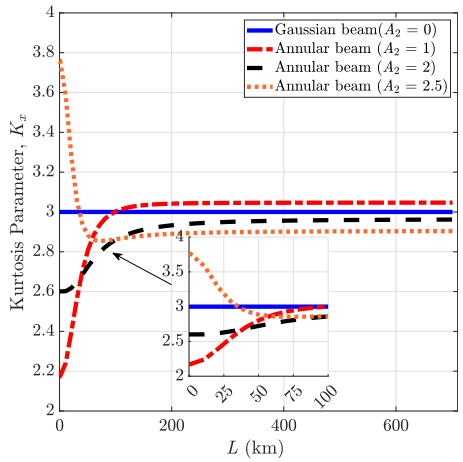

Fig. 12. Kurtosis parameter versus propagation distance L for various secondary field amplitudes A_2 (V/m).

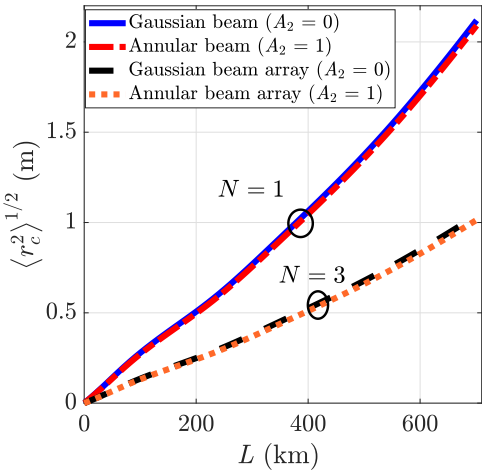

Fig. 13. Beam wander versus propagation distance L for various beam shapes.

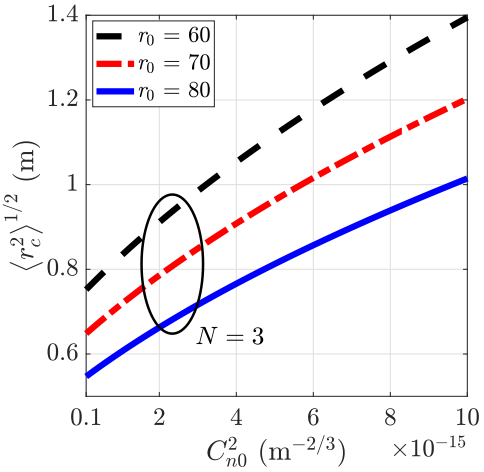

Fig. 14. Beam wander of an annular beam array versus ground-level structure constant C_{n0}^2 for various ring radii at $L = 701$ km.

The dependence of the effective beam spot radius on propagation distance is illustrated in Fig. 8 for various beam shapes: the annular beam array, Gaussian beam array, single annular beam, and single Gaussian beam. As expected, the beam footprint expands with propagation distance in all cases. The annular beam array $N = 3$ produces the largest footprint at a fixed distance, while the Gaussian beam array, single annular beam, and single Gaussian beam follow in descending order of size. Here, we note that the satellite's altitude, h, is determined using the equation $h = L\cos(\zeta^\circ)$. For $L = 701$ km and $\zeta = 30^\circ$ (yielding $h \approx 607$ km), the beam spot radius expands to roughly 3.5 m, leading to a total beam footprint of approximately 7 m for all beam shape configurations. Similarly, Fig. 9 presents the effective beam spot radius of an annular beam array as a function of propagation distance for different secondary field amplitudes A_2. The results indicate that, for a given propagation distance, the beam spot radius enlarges as the secondary field amplitude A_2 increases.

In Fig. 10, the effective beam spot radius versus the number of annular beams N is illustrated for various ring radius values r_0. As observed from Fig. 10, as the number of annular lasers increases, the effective beam spot radius initially decreases, eventually reaching saturation. The saturation of the effective beam spot radius occurs earlier for a beam array with a shorter ring radius compared with those with a longer ring radius. This behavior arises because a ring with a shorter radius requires fewer annular lasers to be positioned. For a constant N, as the ring radius r_0 increases, the beam spot radius also increases as expected. It is important to note that when saturation in the beam spot radius occurs, it indicates that a single large annular beam is formed at the transmitter, with a radius of r_0. This happens because we completely fill the ring with laser sources, creating an appearance similar to an annular shape.

Fig. 11 presents the evolution of the kurtosis parameter as a function of propagation distance for various beam configurations, including annular beam array, Gaussian beam array, single annular beam, and single Gaussian beam. A kurtosis value of $K_x = 3$ corresponds to a Gaussian (Mesokurtic) distribution. The Gaussian beam consistently maintains this value during propagation, making it a suitable reference for comparison. From Fig. 11, we observe the behavior of the proposed laser beams. When the kurtosis falls below 3 (Platykurtic), the beam's distribution exhibits broader tails than a Gaussian. Conversely, a kurtosis above 3 (Leptokurtic) indicates narrower tails compared to the Gaussian distribution. In Fig. 11, we observe that as the propagation distance increases, the kurtosis of annular beam, Gaussian beam array, and the annular beam array increase and approach to the Gaussian distribution. This behavior is expected because, after a sufficiently long propagation distance, a laser beam will evolve into a Gaussian beam distribution, regardless of its initial profile [50], [51]. This phenomenon can also be interpreted through the central limit theorem [4].

Fig. 12 examines the evolution of the kurtosis parameter for a single annular beam as a function of propagation distance, under conditions where the secondary field amplitude is uniformly increased. The results demonstrate that increasing the secondary field amplitude leads to a narrowing of the beam's tail, eventually exceeding the Gaussian kurtosis reference (i.e., $K_x = 3$) at the transmitter, as shown by the orange dashed curve. At a propagation distance of $L = 701$ km, only the annular beam configuration with $A_2 = 1$ maintains a kurtosis value

above 3, indicating a narrower tail than the Gaussian beam. Other field amplitudes yield $K_x < 3$, corresponding to broader tails compared with the Gaussian distribution. The figure demonstrates that for propagation distances under $L = 100$ km, the kurtosis of the single annular beam depends strictly on the A_2 parameter and propagation. During propagation, the beam's tails evolve due to the combined effects of turbulence and diffraction. As detailed in the inset, the beam with $A_2 = 2.5$ initially exhibits narrower tails than the Gaussian beam but broadens by $L = 100$ km. Conversely, the beam with $A_2 = 2$ begins with wider tails and maintains this greater width throughout. The beam with $A_2 = 1$, however, shows a more complex evolution: starting with wider tails, it converges to nearly match the Gaussian profile at $L = 100$ km and is projected to become narrower beyond this point. Note that the Gaussian beam maintains a kurtosis value of 3 throughout propagation, which is a mathematical property of the Gaussian (normal) distribution and serves as a benchmark for other beam types. A kurtosis value of 3 physically reflects that the shape of the tails of the intensity distribution of a Gaussian laser beam under turbulent propagation follows a Gaussian (normal) profile. This occurs because the beam's intensity results from the cumulative effect of turbulence along the propagation path, which, according to the central limit theorem, naturally leads to a Gaussian distribution with kurtosis 3.

In Fig. 13, we plot the beam wander versus the propagation distance for various beam configurations, including annular beam array, Gaussian beam array, single annular beam, and single Gaussian beam. Beam wander refers to the undesired deviation of a beam from its diffraction-limited spot position (i.e., the turbulence-free case). As propagation distance increases, all beams experience stronger turbulence effects, leading to increased beam wander. However, both the Gaussian beam array and annular beam array demonstrate superior beam wander resistance compared with their single-beam counterparts. At a fixed propagation distance L, the annular beam array exhibits slightly better performance than the Gaussian beam array, which in turn outperforms the single annular beam. The single Gaussian beam shows the weakest beam wander resistance among all configurations.

Fig. 14 illustrates the dependence of beam wander on the ground-level structure constant for different ring radii at a propagation distance of $L = 701$ km. As seen in the figure, beam wander increases with a higher ground-level structure constant, while a larger ring radius r_0 helps to reduce the beam wander.

B. Numerical Results for the Scintillation Index and BER

This section presents numerical results for the derived formulations, focusing on the scintillation index and BER under weak atmospheric turbulence. Since the source size given in Table I of Section III-A corresponds to the strong turbulence regime, we instead use relatively smaller annular laser source sizes to remain in the weak turbulence regime. Accordingly, simulations are performed for the primary and secondary source sizes of $\alpha_{s1} = 5$ cm and $\alpha_{s2} = 4.5$ cm, with a ring radius of $r_0 = 8$ cm. Furthermore, unless specified otherwise in the figures, the BER analysis of the laser-satellite link with annular lasers was carried out using the PPM parameters provided in Table II. To validate the scintillation index expression derived in (25), we reduce our formulation to the single annular beam case and observed close agreement with the numerical results reported in [22].

TABLE II
PPM LASER-SATELLITE LINK PARAMETERS

Symbol	Definition	Value
η_q	Quantum efficiency	0.6
R_b	Data bit rate	10 Gbps
ς	APD ionization factor	0.028
M_D	APD current gain	80
T_e	Receiver temperature	300°K
R_L	APD load resistance	50 Ω
M_o	Modulation order	32
A_1	Primary beam amplitude	0.1 V/m
A_2	Secondary beam amplitude	0.1 V/m

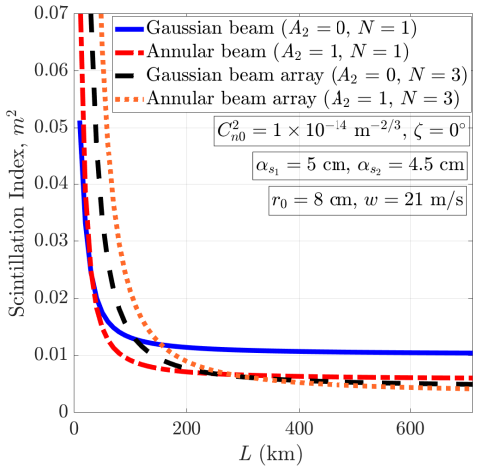

Fig. 15. Scintillation index versus propagation distance L obtained for various beam shapes.

Fig. 15 shows that the scintillation index decreases as the propagation distance increases, which is consistent with the findings reported in [22]. At shorter distances, the Gaussian beam exhibits the lowest scintillation index, followed by the single annular beam, the laser array beam, and finally, the annular beam array, which shows the highest scintillation index. However, beyond a propagation distance of $L = 300$ km, this trend reverses: the annular beam array yields the lowest scintillation index, followed by the Gaussian beam array, the single annular beam, and finally the Gaussian beam, which exhibits the highest scintillation index.

Fig. 16 illustrates the scintillation index versus the number of annular beams, with $N = 1$ being the single annular beam case, where the laser is located at the center ($r_0 = 0$). As the number of annular beams increases, the scintillation index decreases up to $N = 3$, beyond which further increases have little effect. In addition, increasing the ring radius further reduces the scintillation.

Fig. 17 presents the logarithm of the BER versus propagation distance for different values of N. The PPM-related parameters are listed in Table II. As shown in the figure,

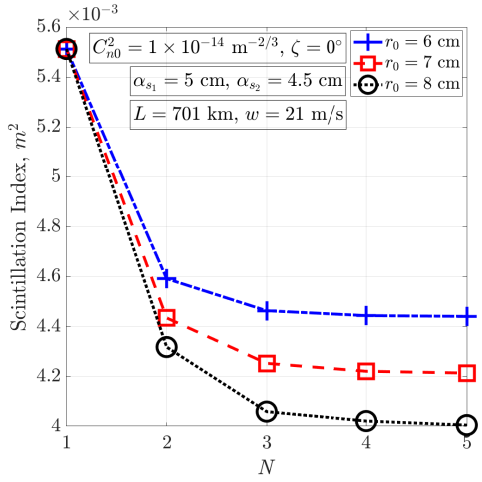

Fig. 16. Scintillation index versus number of annular beams N for various ring radii r_0 values.

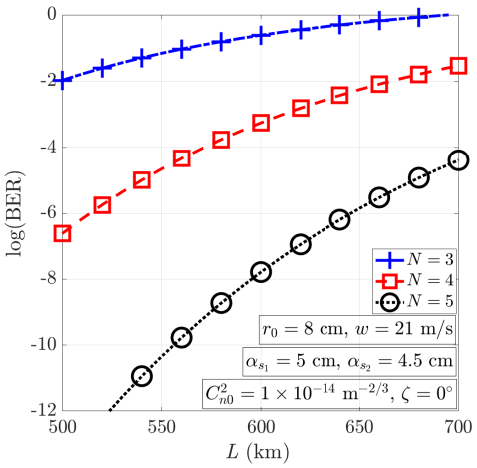

Fig. 17. Logarithm of BER of PPM modulated laser-satellite link versus propagation distance L for various annular beam numbers N.

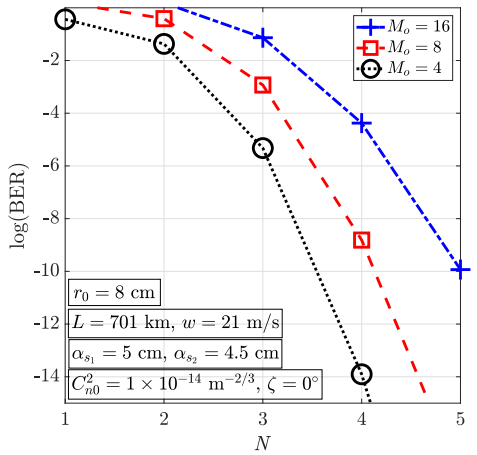

Fig. 18. Logarithm of BER of the laser-satellite link versus the number of annular beams N for various PPM modulation orders M_o.

the BER increases with increasing propagation distance, as expected. This behavior is physically explained by the decrease in intensity at the detector with distance, while the scintillation index remains nearly constant, leading to a significant rise in BER. As the number of annular beams in the array increases, delivering more power to the receiver, BER decreases.

Fig. 18 presents the logarithm of BER versus the number of annular beams N for different modulation orders M_o. As shown, increasing the number of annular beams delivers more power to the receiver, thereby reducing BER. In contrast, higher modulation orders lead to increased BER, since using more time slots per symbol lowers the effective signal-to-noise ratio per slot, making the system more susceptible to noise and atmospheric turbulence, and consequently resulting in higher error rates.

IV. Conclusion

This study presents an analytical derivation of the propagation characteristics of our novel optical beam model, which can be adapted to various beam configurations, including annular beam array, Gaussian beam array, single annular beam, and single Gaussian beam, for uplink laser-satellite communications. The key propagation properties examined for this model include received optical intensity, kurtosis parameter, beam footprint radius, Strehl ratio, and beam wander. A comparative analysis of different optical beams is conducted based on these performance metrics. To analytically evaluate the coherence length required for the Huygens–Fresnel principle, we employ the H–V model, which characterizes the vertical profile of the refractive index structure constant $C_n^2(\eta)$. For the analytical determination of the beam footprint radius, we utilize Carter's definition of beam spot size, based on the $1/e^2$ intensity criterion for Gaussian beams (i.e., the Gaussian beam waist w_0). Furthermore, we adopt an alternative definition of the Strehl ratio to account for the unique propagation characteristics of multiple annular beams. Unlike the conventional approach that compares peak intensities (the ratio of maximum optical intensity with turbulence to the turbulence-free case), we instead define the Strehl ratio as the ratio of the squares of the beam spot radius in free space to that in turbulent conditions. This modified definition is necessary because the propagation of multiple annular beams produces several intensity maxima, making the traditional intensity-based Strehl ratio calculation less meaningful for our beam configurations.

In the study, we observed that increasing both the secondary field amplitude and the ring radius leads to a higher Strehl ratio. However, extending the propagation distance results in a degradation of the Strehl ratio. In addition, as the number of beams in the array increases, the Strehl ratio shows a slight decline before reaching a saturation point. Among all the beams compared, the annular beam array exhibits the highest performance, whereas the single Gaussian beam demonstrates the lowest performance in terms of Strehl ratio. Moreover, increasing the propagation distance, the secondary field amplitude, and the ring radius leads to an enlargement of the beam spot radius at the receiver. Conversely, as the number of beams in the ring increases, the effective beam spot radius experiences a slight decrease.

In this analysis, we measure a kurtosis of 3, verifying the beam's Gaussian (mesokurtic) distribution. The Gaussian beam consistently preserves this value throughout propagation,

making it an appropriate benchmark for comparison. The kurtosis values of beam arrays, whether annular or Gaussian, remain below 3, indicating heavier tails compared with a standard Gaussian distribution. However, the single annular beam exhibits variations in its tail during propagation, becoming alternately wider and narrower compared with the Gaussian beam. In addition, the secondary field amplitude significantly influences the kurtosis value.

Our investigation additionally characterized the beam wander phenomenon exhibited by the proposed optical model under turbulent atmospheric conditions in uplink satellite laser communications. It is found that an increase in the propagation distance and ground-level structure constant causes an increase in the beam wander. However, an increase in the ring radius results in a reduction in the beam wander. The beam wander analysis reveals a clear performance hierarchy: the annular beam array demonstrates superior performance with minimal wander, followed by the Gaussian beam array in second position. The single annular beam ranks third, while the conventional Gaussian beam exhibits the most pronounced wander effects among all tested configurations. The beam array demonstrates a clear advantage in minimizing beam wander.

Finally, we presented the scintillation index and BER performance of the proposed laser source model employing PPM. The results show that the annular beam array yields the lowest scintillation index at propagation distances beyond 300 km. Moreover, increasing the number of beams, which delivers more power to the receiver, reduces BER, while higher modulation orders and longer propagation distances lead to an increase in BER. It should be noted that we did not compare the BER of the annular beam array with that of the Gaussian beam or the Gaussian beam array, since a fair comparison requires equalizing the transmitted power, which may be considered in future work.

This study makes significant contributions to understanding how beam shaping techniques and spatial diversity enhance the propagation performance of transmitted laser beams in uplink satellite communication systems. We believe that the analyses of intensity distribution, Strehl ratio, beam spot radius, kurtosis parameter, beam wander, and scintillation index offer a comprehensive understanding of beam propagation behavior in laser-satellite systems. Moreover, the inclusion of the BER analysis provides valuable insight into how optical wave parameters affect the overall communication performance.

REFERENCES

[1] M. A. Khalighi and M. Uysal, "Survey on free space optical communication: A communication theory perspective," *IEEE Commun. Surveys Tuts.*, vol. 16, no. 4, pp. 2231–2258, 2014.

[2] H. Kaushal and G. Kaddoum, "Optical communication in space: Challenges and mitigation techniques," *IEEE Commun. Surveys Tuts.*, vol. 19, no. 1, pp. 57–96, 1st Quart., 2017.

[3] H. Hemmati, *Deep Space Optical Communications*. Hoboken, NJ, USA: Wiley, 2006.

[4] L. C. Andrews and R. L. Phillips, *Laser Beam Propagation Through Random Media: Second Edition*. Bellingham, WA, USA: SPIE, 2005.

[5] W. P. Latham, "Shaping of annular laser intensity profiles and their thermal effects for optical trepanning," *Opt. Eng.*, vol. 45, no. 1, Jan. 2006, Art. no. 014301.

[6] Z. Song, Z. Liu, J. Ye, Q. Sun, and S. Liu, "Random sources generating far fields with ring-shaped array profiles," *Optik*, vol. 168, pp. 590–597, Sep. 2018.

[7] B. Chen, Q. Wu, Y. Tang, J. Fan, X. Chen, and Y. Sun, "Design of an optical system for generating annular-focused beams using a conical mirror and a parabolic cylindrical mirror," *Optik*, vol. 281, Jun. 2023, Art. no. 170625.

[8] S. Navidpour, M. Uysal, and M. Kavehrad, "BER performance of free-space optical transmission with spatial diversity," *IEEE Trans. Wireless Commun.*, vol. 6, no. 8, pp. 2813–2819, Aug. 2007.

[9] Z. Ghassemlooy, W. Popoola, and S. Rajbhandari, *Optical Wireless Communications: System and Channel Modelling With MATLAB*. Boca Raton, FL, USA: CRC Press, 2019.

[10] C. Fuchs, D. Giggenbach, R. M. Calvo, and W. Rosenkranz, "Transmitter diversity based on phase-division," *Proc. SPIE*, vol. 10096, p. 44, Mar. 2019.

[11] R. K. Tyson and B. W. Frazier, *Principles of Adaptive Optics*. CRC press, 2022.

[12] K. Broekens et al., "Adaptive optics pre-correction demonstrator for terabit optical communication," in *Proc. Int. Conf. Space Opt.*, Jul. 2023, p. 63.

[13] F. E. S. Vetelino and L. C. Andrews, "Annular Gaussian beams in turbulent media," *Proc. SPIE*, vol. 5160, p. 86, Jan. 2004.

[14] F. E. S. Vetelino and R. J. Morgan, "Propagation of higher-order annular Laguerre-Gauss beams in atmospheric turbulence," *Atmos. Propag. VII*, vol. 7685, Apr. 2010, Art. no. 768503.

[15] X. Xiao and D. Voelz, "Annular beam propagation through turbulence: Wave optics study of intensity and scintillation properties," in *Proc. IEEE Aerosp. Conf.*, Mar. 2012, pp. 1–6.

[16] L. Dou, X. Ji, and P. Li, "Propagation of partially coherent annular beams with decentered field in turbulence along a slant path," *Opt. Exp.*, vol. 20, no. 8, pp. 8417–8430, 2012.

[17] X. Li and X. Ji, "Propagation characteristics of decentered annular beams through non-Kolmogorov turbulence," *J. Opt. Soc. Amer. A, Opt. Image Sci.*, vol. 31, no. 1, pp. 172–182, Jan. 2014.

[18] H. Chen, X. Ji, G. Ji, and H. Zhang, "Scintillation characteristics of annular beams propagating through atmospheric turbulence along a slanted path," *J. Opt.*, vol. 17, no. 8, Aug. 2015, Art. no. 085605.

[19] X. Ji, H. Chen, and G. Ji, "Characteristics of annular beams propagating through atmospheric turbulence along a downlink path and an uplink path," *Appl. Phys. B*, vol. 122, no. 8, pp. 1–11, Aug. 2016.

[20] H. Gerçekcioğlu and Y. Baykal, "Annular beam scintillations in non-Kolmogorov weak turbulence," *Appl. Phys. B*, vol. 106, no. 4, pp. 933–937, Mar. 2012.

[21] Y. Chen, Y. Cai, H. T. Eyyuboğlu, and Y. Baykal, "Scintillation properties of dark hollow beams in a weak turbulent atmosphere," *Appl. Phys. B, Lasers Opt.*, vol. 90, no. 1, pp. 87–92, Jan. 2008.

[22] H. Gerçekcioğlu, "Performance of annular beams in weak atmospheric turbulence for satellite laser communications," *Opt. Commun.*, vol. 439, pp. 233–238, May 2019.

[23] H. Gerçekcioğlu and Y. Baykal, "Scintillation and bit error rate in bidirectional laser communications between an aerial vehicle and a satellite using annular optical beams in strong turbulent atmosphere," *J. Opt. Soc. Amer. A, Opt. Image Sci.*, vol. 38, no. 10, pp. 1391–1399, 2021.

[24] H. T. Eyyuboğlu and C. Z. Çil, "Beam wander of dark hollow, flat-topped and annular beams," *Appl. Phys. B*, vol. 93, nos. 2–3, pp. 595–604, Nov. 2008.

[25] H. T. Eyyuboğlu, S. Altay, and Y. Baykal, "Propagation characteristics of higher-order annular Gaussian beams in atmospheric turbulence," *Opt. Commun.*, vol. 264, no. 1, pp. 25–34, Aug. 2006.

[26] H. T. Eyyuboğlu, "Higher order annular Gaussian laser beam propagation in free space," *Opt. Eng.*, vol. 45, no. 4, Apr. 2006, Art. no. 049801.

[27] Y. Zhang, X. Ji, X. Li, Q. Li, and H. Yu, "Self-focusing effect of annular beams propagating in the atmosphere," *Opt. Exp.*, vol. 25, no. 18, pp. 21329–21341, 2017.

[28] Y. Cai, Y. Chen, H. T. Eyyuboğlu, and Y. Baykal, "Propagation of laser array beams in a turbulent atmosphere," *Appl. Phys. B*, vol. 88, no. 3, pp. 467–475, Aug. 2007.

[29] P. Zhou, Z. Liu, X. Xu, and X. Chu, "Propagation of coherently combined flattened laser beam array in turbulent atmosphere," *Opt. Laser Technol.*, vol. 41, no. 4, pp. 403–407, Jun. 2009.

[30] V. Jolivet et al., "Beam shaping of single-mode and multimode fiber amplifier arrays for propagation through atmospheric turbulence," *IEEE J. Sel. Topics Quantum Electron.*, vol. 15, no. 2, pp. 257–268, Mar. 2009.

[31] E. E. Elsayed, "Atmospheric turbulence mitigation of MIMO-RF/FSO DWDM communication systems using advanced diversity multiplexing with hybrid N-SM/OMI M-ary spatial pulse-position modulation schemes," *Opt. Commun.*, vol. 562, Jul. 2024, Art. no. 130558.
[32] Ö. F. Sayan, H. Gerçekcioğlu, and Y. Baykal, "Hermite Gaussian beam scintillations in weak atmospheric turbulence for aerial vehicle laser communications," *Opt. Commun.*, vol. 458, Mar. 2020, Art. no. 124735.
[33] Ö. F. Sayan, H. Gerçekciğlu, and Y. Baykal, "Multimode laser beam scintillations in weak atmospheric turbulence for vertical link laser communications," *Waves Random Complex Media*, vol. 32, no. 4, pp. 1890–1902, Jul. 2022.
[34] W. Du et al., "Scintillation index of a plane wave propagating through Kolmogorov and non-Kolmogorov turbulence along laser-satellite communication downlink at large zenith angles," *J. Russian Laser Res.*, vol. 41, no. 6, pp. 616–627, Nov. 2020.
[35] W. Du et al., "Scintillation index of a spherical wave propagating through Kolmogorov and non-Kolmogorov turbulence along laser-satellite communication uplink at large zenith angles," *J. Russian Laser Res.*, vol. 42, no. 2, pp. 198–209, Mar. 2021.
[36] F. Wang, W. Du, Q. Yuan, D. Liu, and S. Feng, "Wander of a Gaussian-beam wave propagating through Kolmogorov and non-Kolmogorov turbulence along laser-satellite communication uplink," *Atmosphere*, vol. 13, no. 2, p. 162, Jan. 2022.
[37] Y. Baykal, Y. Ata, and M. C. Gökçe, "Underwater turbulence, its effects on optical wireless communication and imaging: A review," *Opt. Laser Technol.*, vol. 156, Dec. 2022, Art. no. 108624.
[38] I. S. Gradshteyn and I. M. Ryzhik, *Table of Integrals, Series, and Products*. New York, NY, USA: Academic, 2014.
[39] L. C. Andrews, R. L. Phillips, and P. T. Yu, "Optical scintillations and fade statistics for a satellite-communication system," *Appl. Opt.*, vol. 34, no. 33, pp. 7742–7751, 1995.
[40] F. Quatresooz and C. Oestges, "C_n^2 modeling for free-space optical communications: A review," *IEEE Access*, vol. 13, pp. 21279–21305, 2025.
[41] R. R. Beland, "Some aspects of propagation through weak isotropic nonkolmogorov turbulence," *Proc. SPIE*, vol. 2375, pp. 6–16, Apr. 1995.
[42] Y. Baykal, "Coherence length in non-Kolmogorov satellite links," *Opt. Commun.*, vol. 308, pp. 105–108, Nov. 2013.
[43] G. Zhou, S. Feng, Y. Xu, and Y. Zhou, "Beam propagation factor and kurtosis parameter of hollow vortex Gaussian beams: An alternative method," *J. Opt. Soc. Amer. A, Opt. Image Sci.*, vol. 36, no. 11, pp. 1908–1916, 2019.
[44] M. C. Gökçe and R. Saathof, "Propagation of vortex beams in atmospheric turbulence for uplink satellite links," *Phys. Scripta*, vol. 100, no. 12, Dec. 2025, doi: 10.1088/1402-4896/ae243a.
[45] Q. Wang, B. Hu, L. Yu, and Y. Zhang, "Strehl ratio and spread rate of Gaussian–Schell model beams in the marine–atmosphere link of weak to strong scintillations," *Optik*, vol. 144, pp. 553–560, Sep. 2017.
[46] W. Wen, X. Chu, and Y. Cai, "Dependence of the beam wander of an airy beam on its kurtosis parameter in a turbulent atmosphere," *Opt. Laser Technol.*, vol. 68, pp. 6–10, May 2015.
[47] Y. Yuan et al., "Beam wander relieved orbital angular momentum communication in turbulent atmosphere using Bessel beams," *Sci. Rep.*, vol. 7, no. 1, p. 42276, Feb. 2017.
[48] Y. Baykal, "Formulation of correlations for general-type beams in atmospheric turbulence," *J. Opt. Soc. Amer. A, Opt. Image Sci.*, vol. 23, no. 4, pp. 889–893, 2006.
[49] H. T. Eyyuboğlu, Y. Baykal, E. Sermutlu, O. Korotkova, and Y. Cai, "Scintillation index of modified Bessel-Gaussian beams propagating in turbulent media," *J. Opt. Soc. Amer. A, Opt. Image Sci.*, vol. 26, no. 2, pp. 387–394, 2009.
[50] Y. Cai and S. He, "Propagation of various dark hollow beams in a turbulent atmosphere," *Opt. Exp.*, vol. 14, no. 4, pp. 1353–1367, 2006.
[51] V. I. Tatarskii, "The effects of the turbulent atmosphere on wave propagation," Israel Program Sci. Translations, Tech. Rep., 1972.

Muhsin Caner Gökçe received the M.S. degree in electronics engineering from Ankara University, Ankara, Türkiye, in 2012, and the Ph.D. degree in electronic and communication engineering from Çankaya University, Ankara, in 2016.

He is an Associate Professor with the Department of Electrical and Electronics Engineering, TED University, Ankara. He is currently employed as a Post-Doctoral Researcher with the Department of Geoscience and Remote Sensing, Delft University of Technology, Delft, The Netherlands. His research interests include optical wireless communication and optical beam propagation through turbulent media.

Rudolf Saathof received the M.Sc. degree in mechanical engineering from the University of Twente, Enschede, The Netherlands, in 2009, and the Ph.D. degree in mechanical engineering from Delft University of Technology, Delft, The Netherlands, in 2013.

He is currently an Assistant Professor with the Department of Space Engineering, Faculty of Aerospace Engineering, Delft University of Technology. His research interests include optomechatronics to improve the optical propagation through turbulence for bidirectional Earth-to-satellite communications.